ACS NANO

www.acsnano.org

ARTICLE

Extracting Pure Circular Dichroism from Hierarchically Structured CdS Magic Cluster Films

Yuan Yao, Thomas J. Ugras, Talisi Meyer, Matthew Dykes, Da Wang, Arantxa Arbe, Sara Bals, Bart Kahr, and Richard D. Robinson*

Cite This: *ACS Nano* 2022, 16, 20457–20469

Read Online

ACCESS | Metrics & More | Article Recommendations | Supporting Information

ABSTRACT: Chiroptically active, hierarchically structured materials are difficult to accurately characterize due to linear anisotropic contributions (i.e., linear dichroism (LD) and linear birefringence (LB)) and parasitic ellipticities that produce artifactual circular dichroism (CD) signals, in addition to chiral analyte contributions ranging from molecular-scale clusters to micron-sized assemblies. Recently, we have shown that CdS magic-sized clusters (MSC) can self-assemble into ordered films that have a hierarchical structure spanning seven orders of length-scale. These films have a strong CD response, but the chiral origins are obfuscated by the hierarchical architecture and LDLB contributions. Here, we derive and demonstrate a method for extracting the "pure" CD signal (CD generated by structural dissymmetry) from hierarchical MSC films and identified the chiral origin. The theory behind the method is derived using Mueller matrix and Stokes vector conventions and verified experimentally before being applied to hierarchical MSC and nanoparticle films with varying macroscopic orderings. Each film's extracted "true CD" shares a bisignate profile aligned with the exciton peak, indicating the assemblies adopt a chiral arrangement and form an exciton coupled system. Interestingly, the linearly aligned MSC film possesses one of the highest *g*-factors (0.05) among semiconducting nanostructures reported. Additionally, we find that films with similar electronic transition dipole alignment can possess greatly different *g*-factors, indicating chirality change rather than anisotropy is the cause of the difference in the CD signal. The difference in *g*-factor is controllable via film evaporation geometry. This study provides a simple means to measure "true" CD and presents an example of experimentally understanding chiroptic interactions in hierarchical nanostructures.

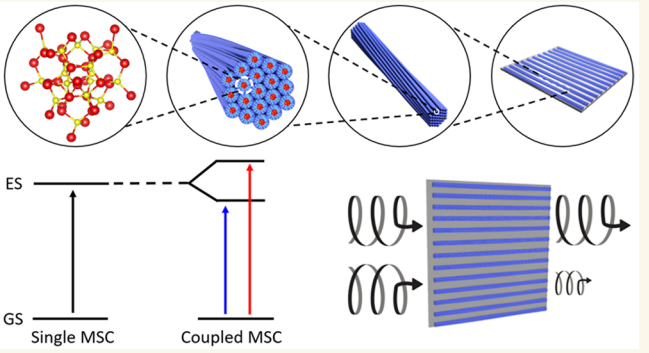

KEYWORDS: *magic-sized cluster, self-assembly, hierarchical nanostructure, anisotropic circular dichroism, Mueller matrix, supramolecular chirality control*

The study of chiroptical activity in inorganic nanosystems is a dynamically growing area[1−5] with potential applications from catalysis and sensing[4] to quantum computation and information technologies.[6] Chiroptic activity—which is manifested as the preferential absorption or dispersion of circularly polarized light—emanates from suitably dissymmetric materials, albeit not necessary chiral.[7,8]

Circular dichroism (CD) spectroscopy[9] is widely used for the detection and quantification of chiroptic activity by measuring the differential absorption of left- and right-handed circularly polarized light. The main shortcoming with all CD measurements is that materials with macroscopic anisotropies can have undesired contributions to the signal from the linear dichroism (LD) and linear birefringence (LB) and the residual static birefringence (imperfection) of photoelastic modulators that are used to modulate between left and right circular polarization states.[10,11] These collective contributions have been termed "apparent CD" or "pseudo CD".[2,10] The intensity of the "chiroptic-CD" signal (also known as "true CD") that is generated from the coupling between the transition electronic dipole and transition magnetic dipole can be orders of

Received: July 7, 2022
Accepted: November 3, 2022
Published: November 17, 2022

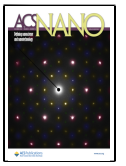

https://doi.org/10.1021/acsnano.2c06730
ACS Nano 2022, 16, 20457−20469

magnitude smaller than linear anisotropy-induced CD signals (which are generated solely from electronic dipole-allowed transitions).[2,12] It is important to note that the necessary condition for CD in an isotropic solution is chirality, but this is not the case for oriented materials: the chiroptic-CD signal (true CD) can be nonzero in an achiral system that is highly oriented.[8] In these cases, the coupling between the electronic transition dipoles and magnetic transition dipoles or electric quadrupoles still produces the CD signal, but the chromophore is achiral. Here, the term chiroptic-CD refers to this true CD, whether in achiral or chiral systems.[8]

The effects of oriented systems have been studied for decades,[10,13] with the most popular work coming from Shindo et al., who developed the theoretical model for understanding how oriented samples can show significant CD signals due to the simultaneous presence of LD and LB.[10,14,15] Recent studies have shown the interaction between LD and LB could lead to the reversal of the CD signal when the wave vector ($\vec{k}$) of the incident light is reversed, known as "non-reciprocal" CD or polarity reversal of ellipticity.[15,16] While the methods to remove these linear anisotropies have been varied, they mostly involve the averaging of signals at different azimuthal angles (rotations around the incident beam typically in 15° or 30° increments) in addition to measurements of $\pm \vec{k}$.[17−19] Using these methods, the chiroptic-CD has been extracted from the linear anisotropy-induced CD in simple systems, such as plasmonic nanoparticles embedded in a film.[19] An area that remains relatively unexplored identifies the chiroptical origin in complex hierarchical structures, such as architectures that are highly oriented across different length scales.[20] Studying the chiroptic activity in complex hierarchical structures will help us understand chiral light−matter interactions at different length scales and facilitates the future design of complex chiroptical devices. These studies, however, have not previously been performed due to the synthetic complexity of creating a hierarchical structure that can be probed optically, extracting the contributions of different optical processes, and differentiating contributions to the polarization state of light from nanometer-scale chiral molecules to micron-scale chiral assemblies and chiral surface topology to chiral ligands.[1,21−25]

We have previously reported on a complex hierarchical system where the fundamental units are ∼1.5 nm CdS magic-sized clusters (MSCs) that are arranged hexagonally within linear filaments of an organic mesophase (Figure 1a).[20,21] The radial spacing between adjacent clusters is ∼3.4 nm. The filaments themselves have a radius larger than ∼100 nm and lengths ranging in the 10s to 100s of microns. They twist together into cables with self-limiting widths.[26] Through controlled evaporation speeds and geometries, cables can form linearly aligned macroscopic bands deposited by the stick−slip process.[27] The bands are ordered up to centimeter-scale lengths, completing a hierarchical architecture that spans seven orders of magnitude (Figure 1b). The level of linear alignment can be regulated through changes to deposition and evaporation.[27] Thus, this material system is an ideal testbed to examine the influences of self-assembled alignment on linear anisotropy-induced CD signals, and further, investigate the best methods to decouple chiroptic-CD from linear anisotropy interference.

In this work, we isolate the chiroptic-CD from the linear anisotropy-induced CD in a material with several levels of hierarchical structure. First, using Mueller matrices and Stokes parameters, we derive a simplified four-scan method to

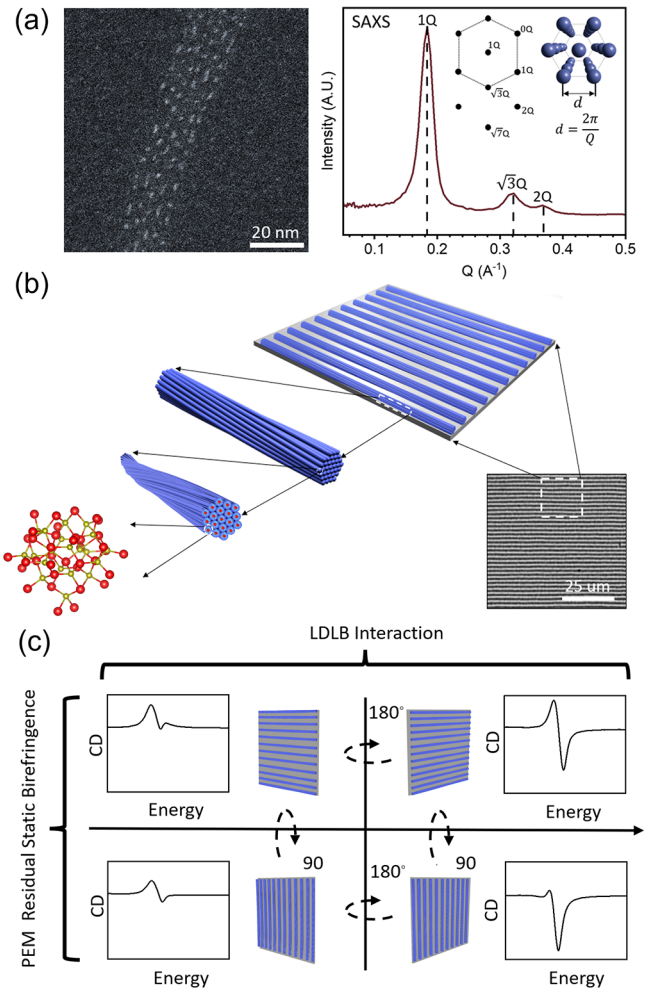

Figure 1. Scanning transmission electron microscope (STEM) image, small-angle X-ray scattering (SAXS) data, and schematics describing the hierarchical structure in the MSC films and the four-scans averaging method for extracting the chirality-induced CD signal. (a) (Left) High-angle annular dark-field scanning transmission electron microscopy (HAADF-STEM) image of a magic size cluster filament with individual clusters appearing as bright dots. (Right) SAXS data of magic size cluster film reveals hexagonal packing of the clusters. The first peak, 1Q, at 0.18 A^{-1} corresponds to a cluster-to-cluster nearest neighbor distance of 3.4 nm. The second and third peaks at 0.32 and 0.37 A^{-1} match the $\sqrt{3}Q$ and 2Q distances from the hexagonal packing. Inset shows the real to reciprocal space conversion. (b) A linearly aligned MSC film is built from ∼1.5 nm MSC that are arranged hexagonally into micron-sized filaments. The filaments twist into cables, and the controlled, ordered alignment of cables yields a centimeter-scale linearly aligned film (at right, optical micrograph of linear film). The film shows preferential absorption of left- or right-circularly polarized light. (c) CD is measured at four orientations (0°, 90° rotation along azimuthal angles, and 0°, 180° rotation along vertical axis). The differences in the CD signal as the sample azimuthal angle is varied are caused by parasitic ellipticities in the photoelastic modulator (PEM). The CD difference along the vertical axis rotation is caused by products of LD and LB when the principal axes of these anisotropies are misoriented.

decouple the chiroptic-CD signal from the CD contributions that are present due to the LDLB interaction and the PEM imperfection (Figure 1c). We apply the four-scan method to CD and LD standards to test its efficacy, and we compare the method to more traditional multiple-rotation scan methods,

https://doi.org/10.1021/acsnano.2c06730
ACS Nano 2022, 16, 20457−20469

finding that the four-scan method provides a more simplified and effective pathway to extract the chiroptic-CD signal. Next, we evaluate the linear anisotropy contributions to CD in hierarchically structured magic-sized cluster films. We compare linearly aligned, radially aligned, spin-coated, and freely evaporated MSC films and find they all share the same bisignate exciton coupling profile and therefore have the same chiroptical origin from the chiral assembly of MSC. In these systems, we find that films produced under a controlled evaporation process (linearly and radially aligned film) show a higher reduced LD and *g*-factor, but the amount of linear order is not in direct correlation with the *g*-factor. In fact, linearly aligned films with a similar electronic transition dipole alignment can manifest an order of magnitude difference in the *g*-factor, which indicates that the evaporation conditions can greatly affect the chirality of the cluster or the cluster assembly. Finally, we compare linearly aligned MSC films with 5 nm CdS nanoparticle films and conclude surface ligands are not contributing to the chiroptic signal.

RESULTS/DISCUSSION

Derivation. To decouple the chiroptic-CD from other linear anisotropic effects, we have adapted the derivation by Shindo and Nishio[10] with the Stokes–Mueller matrix polarimetry by Arteaga et al.[28] The sample can rotate around the axis defined by the incident light direction through an angle of θ and along the axis perpendicular to the incident light direction through an angle of β (Figure 2). The full derivation of our method is detailed below.

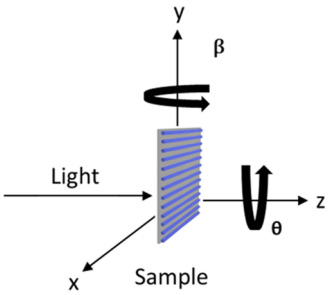

Figure 2. Schematic of the instrumental setup used to measure CD and LD for decoupling the chiroptic-CD contribution. Rotations of the samples can be made through the azimuthal angle θ defined by the incident light vector, which is in the *z*-direction, and around the *y*-axis, perpendicular to the beam direction through the angle β.

Incident light can be described by the Stokes vector (S), which is a 4 × 1 matrix made from components of the electric field of the incident light propagating in the *z*-direction:[28]

$$S = \begin{bmatrix} I \\ Q \\ U \\ V \end{bmatrix} = \begin{bmatrix} |E_x|^2 + |E_y|^2 \\ |E_x|^2 - |E_y|^2 \\ 2E_xE_y \cos\phi \\ 2E_xE_y \sin\phi \end{bmatrix} = \begin{bmatrix} I = I_x + I_y \\ I_x - I_y \\ I_{45^\circ} - I_{-45^\circ} \\ I_R - I_L \end{bmatrix} \quad (1)$$

- I: total intensity of *x*- and *y*-polarized light (I_x, I_y)
- Q: difference in intensities between *x*- and *y*-polarized light
- U: difference in intensities between light polarized at ±45° relative to the *x*-axis (I_{45°, I_{-45°)
- V: difference in intensities between left- and right-circularly polarized light (I_L, I_R)
- E_x and E_y: components of the electric field amplitude in the *x*- and *y*-directions
- ϕ: phase shift between the *x*- and *y*-modes.

For example, linearly polarized E_x light can be expressed by a Stokes vector:

$$S_0 = [1, 1, 0, 0] \quad (2)$$

The Mueller matrix (M_z) is a 4 × 4 matrix that is used to describe the effect of a system on the incident light (S_{in}), yielding the output light, $S_{out} = M_z S_{in}$. To calculate the general Mueller matrix of a sample with a path length of z, we apply the lamellar approximation for light propagating through a homogeneous medium.[28,29] This method assumes that the total optical effect of a medium is the sum of many layers with a width Δz (Figure 3). The Stokes vectors at position z and z + Δz are related by $S(z + \Delta z) = M_{z,\Delta z} S(z)$ where $M_{z,\Delta z}$ is the Mueller matrix of an incremental layer of the medium of thickness Δz located at z.[30] Subtracting $S(z)$ from both sides gives

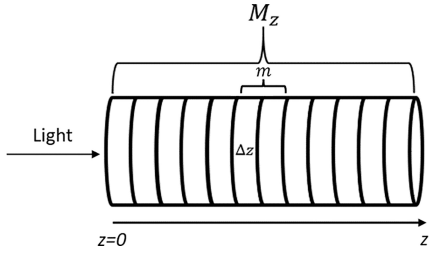

Figure 3. Schematic showing the entire sample and individual slices of the Mueller matrix.

$$\begin{aligned} &S(z + \Delta z) - S(z) \\ &= M_{z,\Delta z} S(z) - S(z) \\ &= (M_{z,\Delta z} - \mathbb{I}) S(z) \end{aligned}$$

where $\mathbb{I}$ is the 4 × 4 identity matrix. Dividing both sides by Δz and taking the limit as $\Delta z \to 0$ results in[28]

$$\frac{dS(z)}{dz} = mS(z) \quad (3)$$

with m defined as the differential propagation matrix of the medium in the Stokes vector-Mueller matrix formulation,

$$m = \lim_{\Delta z \to 0} \frac{M_{z,\Delta z} - \mathbb{I}}{\Delta z} \quad (4)$$

The Stokes vector $S(z)$ at any point, z, is expressed as the incident Stokes vector light, $S_{in} = S(0)$ at $z = 0$, transformed by the Mueller matrix as[30]

$$S(z) = M_z S(0) \quad (5)$$

Eq 5 has the same general solution as eq 3 and adheres to the initial condition $S(z = 0) = S_{in}$, which implies that the initial Mueller matrix slice is $M_0 = \mathbb{I}$ (the identity matrix). Differentiating eq 5 results in

https://doi.org/10.1021/acsnano.2c06730
ACS Nano 2022, 16, 20457–20469

$$\frac{dS(z)}{dz} = \left(\frac{dM_z}{dz}\right)S(0) \tag{6}$$

Substituting in $\frac{dS}{dz}$ from eq 3 gives

$$mS(z) = mM_zS(0) = \left(\frac{dM_z}{dz}\right)S(0) \tag{7}$$

Dividing by $S(0)$ gives

$$mM_z = \left(\frac{dM_z}{dz}\right) \tag{8}$$

And rearranging

$$mdz = M_z^{-1}dM_z \tag{9}$$

Integrating eq 9 gives the Mueller matrix of a sample of thickness z as[30]

$$M_z = e^{mz} \tag{10}$$

The differential Mueller matrix (m) is composed of four fundamental optical effects: linear dichroism (LD), linear birefringence (LB), circular dichroism (CD), circular birefringence (CB), their counterparts (LD′, LB′) measured at 45° relative to the original coordinate system, and the absorbance (A)[28,29]

$$m = \begin{bmatrix} A & -\mathrm{LD} & -\mathrm{LD}' & \mathrm{CD} \\ -\mathrm{LD} & A & \mathrm{CB} & \mathrm{LB}' \\ -\mathrm{LD}' & -\mathrm{CB} & A & -\mathrm{LB} \\ \mathrm{CD} & -\mathrm{LB}' & \mathrm{LB} & A \end{bmatrix} = A\mathbb{I} + \begin{bmatrix} 0 & -\mathrm{LD} & -\mathrm{LD}' & \mathrm{CD} \\ -\mathrm{LD} & 0 & \mathrm{CB} & \mathrm{LB}' \\ -\mathrm{LD}' & -\mathrm{CB} & 0 & -\mathrm{LB} \\ \mathrm{CD} & -\mathrm{LB}' & \mathrm{LB} & 0 \end{bmatrix} = A\mathbb{I} + F \tag{11}$$

Employing the Campbell–Baker–Hausdorff theorem

$$M_z = e^{mz} = e^{A\mathbb{I}z+Fz} = e^{Az}e^{Fz} \tag{12}$$

Expanding the e^{Fz} to the second order is typically sufficient for a moderately anisotropic sample, resulting in[10]

$$e^{Fz} = \mathbb{I} + Fz + \frac{1}{2}F^2z^2 \tag{13}$$

Substituting the matrix F into the above expression, we can obtain the fully expanded matrix M_z as

$$M_z = e^{Az}\begin{bmatrix} 1+0.5z^2(CD^2+LD^2+LD'^2) & -zLD+0.5z^2(-CDL+CBLD') \\ -zLD+0.5z^2(CDLB'-CBLD') & 1+0.5z^2(-CB^2+LD^2-LB'^2) \\ -zLD'+0.5z^2(-CDL+CBLD) & -zCB+0.5z^2(LBLB'+LDLD') \\ zCD+0.5z^2(LDLB'-LBLD') & -zLB'+0.5z^2(-CBLB-CDLD) \end{bmatrix}$$
$$\begin{bmatrix} -zLD'+0.5z^2(CDLB-CBLD) & zCD+0.5z^2(-LDLB'+LBLD') \\ zCB+0.5z^2(LBLB'+LDLD') & zLB'+0.5z^2(-CBLB-CDLD) \\ 1+0.5z^2(-CB^2-LB^2+LD'^2) & zLB+0.5z^2(-CBLB'-CDLD') \\ -zLB+0.5z^2(-CBLB'-CDLD') & 1+0.5z^2(CD^2-LB^2-LB'^2) \end{bmatrix} \tag{14}$$

As the sample can rotate around the vector defined by the incident light propagation direction (θ of Figure 2), a rotation matrix can be applied to the Mueller matrix as[10]

$$S_{out} = R(-\theta)M_zR(\theta)S_{in} = M'(\theta)S_{in} \tag{15}$$

where the rotation matrix is

$$R(\theta) = \begin{bmatrix} 1 & 0 & 0 & 0 \\ 0 & \cos(2\theta) & \sin(2\theta) & 0 \\ 0 & -\sin(2\theta) & \cos(2\theta) & 0 \\ 0 & 0 & 0 & 1 \end{bmatrix} \tag{16}$$

To obtain S_{in} for the CD measurements, we need to create an expression for the incoming light used in a CD instrument. This can be found by calculating the Stokes vector of linearly polarized light (S_0) after being processed into a photoelastic modulator (PEM) operating at frequency f = 50 kHz oriented at 45° to the vertical.[28] S_{in} is then

$$S_{in} = R\left(-\frac{\pi}{4}\right)M_{PEM}R\left(\frac{\pi}{4}\right)S_0 \tag{17}$$

- R: rotation matrix
- M_{PEM}: Mueller matrix for the PEM

$$M_{PEM} = \begin{bmatrix} 1 & 0 & 0 & 0 \\ 0 & 1 & 0 & 0 \\ 0 & 0 & \cos(\delta) & \sin(\delta) \\ 0 & 0 & -\sin(\delta) & \cos(\delta) \end{bmatrix} \tag{18}$$

where δ is given by

$$\delta = A\sin(2\pi ft + \varphi) + \alpha \tag{19}$$

- δ: phase shift of the PEM,
- α: residual static birefringence of the PEM,
- t: time,
- A: general amplitude,
- φ: general phase,
- f: frequency of the PEM.

After substitution, we obtain the Stokes vector for the light coming out of the PEM that is incident on the sample

$$S_{in} = [1, \cos(\delta), 0, \sin(\delta)] \tag{20}$$

Substituting in S_{in} and $M'(\theta)$ into eq 15, we obtain the Stokes vector for the output light S_{out} (see Supporting Information). An idealized detector will detect only the first component of the S_{out},[31] which is

$$I_{detect} = e^{Az}\left\{1 + \frac{1}{2}z^2(\mathrm{CD}^2 + \mathrm{LD}^2 + \mathrm{LD}'^2) + \sin(\delta)\left(z\mathrm{CD} + \frac{1}{2}z^2(-\mathrm{LDLB}' + \mathrm{LBLD}')\right) + \cos(\delta)\left[-\sin(2\theta)\left(\frac{1}{2}(\mathrm{CDLB} - \mathrm{CBLD})z^2 - z\mathrm{LD}'\right) + \cos(2\theta)\left(-z\mathrm{LD} + \frac{1}{2}z^2(-\mathrm{CDLB}' + \mathrm{CBLD}')\right)\right]\right\} \tag{21}$$

There are three terms in this equation; the first of these is direct current (I_{dc}), which is isolated by a lock-in amplifier. The second ($\sin(\delta)$) and third ($\cos(\delta)$) terms are alternating current (I_{ac}) and are processed by a lock-in amplifier, separating the phase-dependent and phase-independent terms from one another. The final CD signal I_{CD} is proportional to $\frac{I_{ac}}{I_{dc}}$ (details of this derivation are in the Supporting Information) and can be expressed as

https://doi.org/10.1021/acsnano.2c06730
ACS Nano 2022, 16, 20457−20469

$$I_{CD} = G_0\left\{zCD + \frac{1}{2}z^2(-LDLB' + LBLD') + \alpha\left[\sin(2\theta)\left(\frac{1}{2}(CDLB - CBLD)z^2 - zLD'\right) + \cos(2\theta)\left(-zLD + \frac{1}{2}z^2(-CDLB' + CBLD')\right)\right]\right\} \quad (22)$$

- $G_0 = c\frac{e^{Az}}{2}J_1(A)V_{\text{lock-in}}$
- $c = \cos(\varphi_{\text{signal}} - \varphi_{\text{lock-in}})$
- $V_{\text{lock-in}}$: lock-in frequency

This final form of the detected signal (eq 22) is composed of the following three components:

The chiroptic-CD signal

$$zCD \quad (23)$$

LDLB interaction terms

$$\frac{1}{2}z^2(-LDLB' + LBLD') \quad (24)$$

and the PEM residual static birefringence terms

$$\alpha\left[\sin(2\theta)\left(\frac{1}{2}(CDLB - CBLD)z^2 - zLD'\right) + \cos(2\theta)\left(-zLD + \frac{1}{2}z^2(-CDLB' + CBLD')\right)\right] \quad (25)$$

In summary, we can express the three major components that contribute to the CD signal measured on a common CD instrument as

$$CD_{\text{measured}} = CD_{\text{chiroptic}} + CD_{\text{LDLB}} + CD_{\alpha} \quad (26)$$

where $CD_{\text{chiroptic}}$ is the chiroptic-CD, CD_{LDLB} is the CD signal generated by the LDLB interaction, and CD_{α} is the CD signal generated by the residual static birefringence of the PEM.

The LDLB interaction term (CD_{LDLB}) arises when the LD and LB principal axes do not align.[2,32] As demonstrated in Figure 4, flipping the sample (rotation along β by 180°) will change the sign of α_{12} which causes sign inversion for the LDLB interaction terms. Therefore, averaging measurements before and after flipping the sample along the incident beam direction will average the CD_{LDLB} to zero.[28]

As for CD_{α}, rotating the sample along θ by 90° will result in two terms that cancel out due to the presence of the $\sin(2\theta)$ and $\cos(2\theta)$ in eq 25. Thus, averaging two measurements, one at θ = 0° and another with the sample rotated at θ = 90°, will average out the CD signal from PEM imperfection.

In summary, both the contributed CD signals from the LDLB interaction and the PEM imperfection show antisymmetric properties upon rotation along their respective axes. We can make use of these antisymmetric properties to remove the contribution of linear anisotropies to our CD signal by measuring four different orientations, (1) θ = 0°, β = 0° (2) θ = 90°, β = 0° (3) θ = 0°, β = 180°and (4) θ = 90°, β = 180° and averaging over the four scans.

Experimental Verification of the Four-Scan Averaging Method. To confirm the capability of the four-scan averaging method, we measure three control samples: quartz as an LD standard, 1S-(+)-10-camphorsulfonic acid ammonium salt films as a CD standard, and a linearly aligned CdS MSC film which has both LD and CD (see detailed discussion in Supporting Information and Figures S1–S6). The four-scan averaging successfully removes the linear anisotropy-induced CD contribution that is present in the raw data of these samples. We also compare our method to the traditional 15° increment (seven-scan) averaging method and prove they produce nearly identical results.

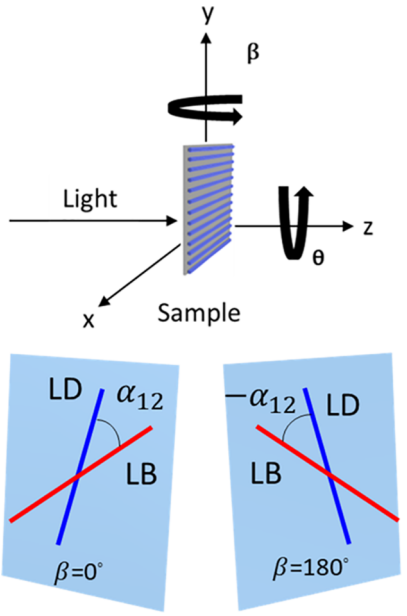

Figure 4. Schematic showing the inversion of the angle between the LD and LB transition dipoles after flipping the sample. Blue and red lines are used to represent the transition dipoles for LD and LB, respectively.

Results from the LD standard show that there is a significant nonzero CD signal (as well as an LD signal) (Figure S1, CD in (a) and LD in (c)). Two-scan and seven-scan averaged spectra result in an identical CD profile, which is constant (at ∼2 mdeg) over the wavelength range, proving that averaging over only two scans at azimuthal angles of θ = 0° and θ = 90° is sufficient to remove the CD contribution introduced from the PEM imperfection (Figure S1b, red and blue plots). With the additional β = 0°, and β = 180° measurements, the four-scan averaging method further reduces the absolute CD intensity to below 1 mdeg (Figure S1b, gray, S2).

Results from the CD standard indicate that the variations in CD intensity and the nonzero LD signal in the raw data (Figure S4, CD in (a) and LD in (c)) are resolved by all three averaging methods (Figure S4b). Comparing the seven-scan averaging (Figure S4b, red) to the two-scan averaging (blue) and the four-scan averaging (gray) finds no difference between the CD signals. The fact that the four-scan averaged CD and LD spectra are identical to the two-scan averaged spectra indicate there are negligible LDLB contributions.

We also compare the seven-scan, two-scan, and four-scan averaging methods on CdS MSC films that have linear alignment (Figure S6, raw data CD in (a) and LD in (c), and averaged data CD in (b) and LD in (d)). The seven-scan and two-scan averaged CD spectra follow the same bisignate profiles with a small difference in the maximum intensity (+57 mdeg to −27 mdeg vs +72 mdeg to −36 mdeg). The four-scans averaged CD also follows the same bisignate profile but

https://doi.org/10.1021/acsnano.2c06730
ACS Nano 2022, 16, 20457−20469

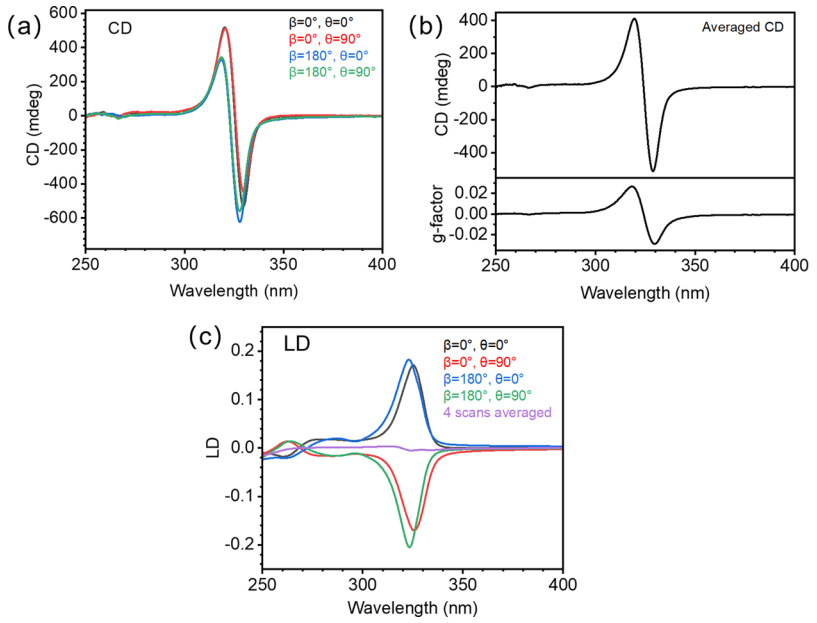

Figure 5. CdS MSC film four-scans averaged CD and LD results. (a) CD results at four orientations show large variations of the CD signal which demonstrates the linear anisotropy contributions. (b) Four-scan averaged CD ("True CD") and *g*-factor results follow the same bisignate profile. CD ranges from +414 to −504 mdeg, and *g*-factor range from 0.027 to −0.030. (c) LD scans at four orientations show rotating the sample 90° along the azimuthal angle leads to reversal of the LD signal. Flipping the sample perpendicular to the beam direction (β = 180°) leads to small or no change of the LD results. Averaging the four spectra yields a spectrum with a 324 nm peak value of 0.005.

has a more intense negative peak at 330 nm (Figure S6b). Importantly, the difference in negative peak intensity between the four-scan and the other two averaging methods is due to the removal of the CD contribution from the LDLB interaction (removal facilitated through the additional β-angle flipping) in the four-scans averaged method. This result illustrates the importance of removing the LDLB and PEM contributions to the raw data to reveal the true expression of the signal.

Circular Dichroism in Hierarchically Structured Films. We study CdS magic-sized cluster films with hierarchical structures varying from nanostructures (nm) to macroscale order (cm). Through four-scan averaging, we isolate the chiroptic-CD signal, LDLB interaction, and CD signal from PEM imperfection. We characterize the chiroptic properties and linear anisotropy of (1) linearly aligned MSC films, (2) radially aligned MSC films, (3) spin-coated MSC films, (4) freely evaporated MSC films, and (5) linearly aligned 5 nm CdS nanoparticle films. Films made with the same batch of MSC solution can result in an opposite couplet profile; both enantiomers (handedness) have been observed from the films. To simplify our study and focus on the *g*-factor comparison, all samples we show in this manuscript share the same handedness (with the couplet having a CD maximum at shorter wavelengths and a CD minimum at longer wavelengths). An example of MSC films with opposite handedness is shown in SI Figure S7.

Linearly Aligned Films. In a previous study, we found that geometrically controlled evaporation of CdS magic-sized clusters can produce highly structured films, and these films have a bisignate CD signal centered at 324 nm.[27] The CD signal also has a strong angular dependence when rotating the sample perpendicular to the beam direction (azimuthal angle θ), indicating a considerable CD contribution from the PEM static birefringence.

Application of the four-scan method to the linearly aligned MSC film quantitatively demonstrates the linear anisotropy contribution to the CD signal, and the averaging enables us to extract the chiroptic-CD signal. The θ-angle averaging removes the CD contribution from the PEM imperfection, and the β-angle averaging removes the LDLB interaction. CD measurements at the four orientations (Figure 5a, top) show the same bisignate profile with varying CD intensities. For example, at θ = 0°, β = 0°, the CD spectrum has a maximum of 524 mdeg and a minimum of −520 mdeg, whereas at θ = 0°, β = 180°, the CD spectrum has a maximum of 332 mdeg and a minimum of −618 mdeg. The four-scan averaged CD spectrum results in a bisignate profile with a maximum of 414 mdeg at 318 nm, a zero-crossing at 324 nm, and a minimum of −504 mdeg at 330 nm (Figure 5b). The four-scan averaged *g*-factor (or the dissymmetry factor, which is the CD signal normalized by absorbance and can be used to quantify the relative chiroptic strength) is 2.7×10^{-2} at 318 nm and -3.0×10^{-2} at 330 nm.

All LD configurations result in a strong, single positive or negative peak at 324 nm depending on the θ orientation (0° or 90°) (Figure 5c). When θ = 0° and β = 0°, a positive LD signal is observed with a maximum intensity of 0.170. After 90° rotation azimuthally, the LD signal inverts with a peak intensity of −0.168. The small intensity difference between these two measurements is caused by a small misalignment during sample rotation. The LD variation between 180° β-angle flip measurements is due to the change in the sample's Mueller matrix depending on whether light goes through the substrate or the MSC film first. Averaging the LD signal over four orientations significantly reduces the peak intensity from 0.170 (θ = 0°, β = 0°) to 0.005 at 324 nm, which confirms the accuracy of our sample alignment and rotation (Figure 5c, purple). Linear dichroism can emanate from several sources, but for absorptive dichroic polarizers—the most common linear polarizer—the optical polarization is caused by the linear alignment of electronic transition dipoles.[33] Because the LD is only present around the exciton absorption wavelength, the alignment of the electronic transition dipoles of the MSCs is

https://doi.org/10.1021/acsnano.2c06730
ACS Nano 2022, 16, 20457−20469

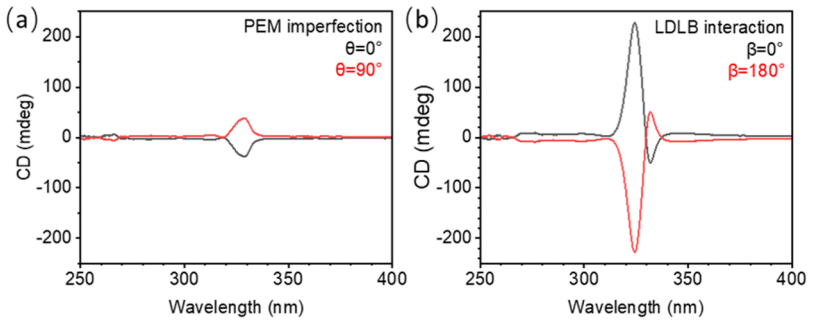

Figure 6. CD components from the LDLB interaction and the PEM imperfection, extracted from the CD four-scan data. (a) Isolated θ-dependent contributions (PEM imperfection) at θ = 0° and 90° show antisymmetric behavior with a peak reaching 39 and −39 mdeg. (b) Isolated β-dependent contributions (LDLB interaction) at β = 0° and 180° also shows an antisymmetric profile with peaks reaching 231 and −231 mdeg. The CD signal from the PEM imperfection is 1/6 of the CD contribution from the LDLB interaction.

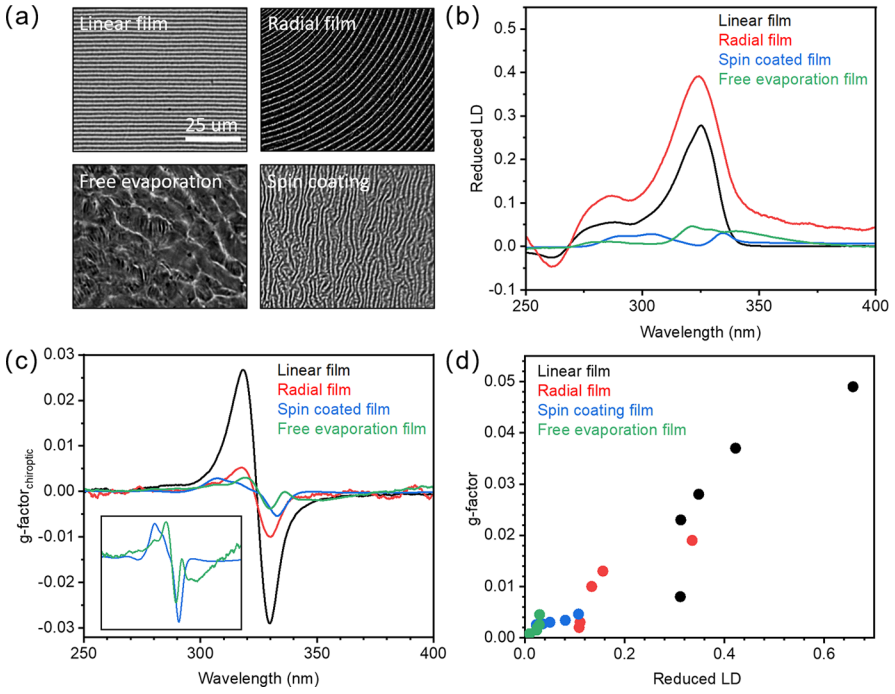

Figure 7. Effects of varying order on reduced LD and $CD_{chiroptic}$. (a) Optical micrographs for linear, radial, spin-coated, and freely evaporated films. (b) Reduced LD (LD normalized by absorbance, LD_{red}) for the four different films. These plots indicate that the radial and linear films have an order of magnitude greater reduced LD (0.39 and 0.27, at maximum) compared to the less-aligned freely evaporated and spin-coated films (0.04 and 0.03, at maximum). (c) The *g*-factor calculated from four-scan averaged CD for the four films. All the *g*-factor curves have similar bisignate line shapes. Inset is the magnified CD data of the spin coated and free evaporation films. (d) Calculated $|g_{max}|$ intensity (four-scans averaged) and reduced LD plotted for 20 films (five films in each category). Films produced under controlled evaporation (linearly and radially aligned films) show higher reduced LD and *g*-factor (dissymmetry) compared to films made under less controlled processes (spin coating and free evaporation films). (It is important to note that the influence of the LDLB and PEM imperfection has been removed from the *g*-factor values.)

the source of the LD, indicating our MSCs are aligned in the film.

The measured CD signal can be separated into the PEM residual static birefringence term, CD_α (defined in eq 22), which is θ-dependent, and an LDLB interaction term, CD_{LDLB}, which is β-angle dependent, that add to the chirality-induced signal $CD_{chiroptic}$.

$$CD_{measured} = CD_{chiroptic} + CD_{LDLB} + CD_\alpha \quad (26)$$

With some simple algebra (shown in Supporting Information), we can solve for CD_{LDLB} and CD_α terms:

$$CD_{LDLB,\beta=180^\circ} = [CD_{(\theta=0^\circ,\beta=180^\circ)} + CD_{(\theta=90^\circ,\beta=180^\circ)} - 2CD_{four\text{-}scans\ averaged}]/2 \quad (27)$$

With similar algebra, we can solve for the other CD_{LDLB} interaction term and both PEM terms, CD_α, for example

$$CD_{\alpha,\theta=0^\circ} = [CD_{(\theta=0^\circ,\beta=0^\circ)} + CD_{(\theta=0^\circ,\beta=180^\circ)} - 2CD_{four\text{-}scans\ averaged}]/2 \quad (28)$$

The calculated CD signals from the LDLB interaction terms and the PEM imperfection terms are shown in Figure 6 for different orientations. Mirror images of the CD signals are

https://doi.org/10.1021/acsnano.2c06730
ACS Nano 2022, 16, 20457−20469

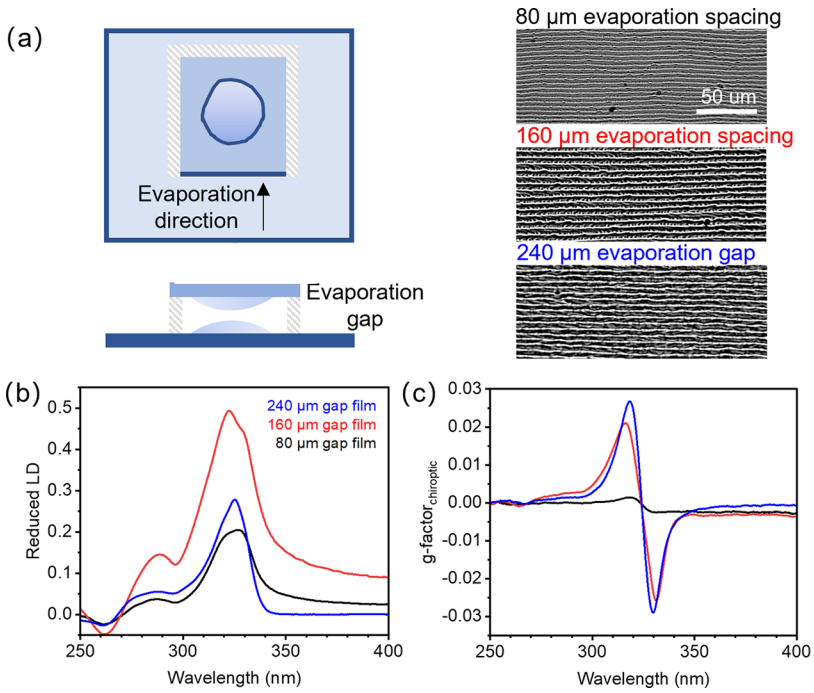

Figure 8. *g*-Factor comparison between different linearly aligned films made with varying evaporation gaps. (a) Schematic showing linearly aligned film evaporation process can be controlled by change the spacing between top and bottom glass slides. Optical micrographs show all films share the same linear pattern. (b) Reduced LD for all three films displays a major peak at 324 nm and a minor peak at 288 nm. The films made with 80 μm (G80) and 240 μm (G240) evaporation gaps have similar maximum intensities of 0.21 and 0.27. The 160 μm evaporation gap (G160) film shows a higher reduced LD maximum of 0.50. (c) *g*-factor (four-scans averaged) plotted for films with different spacing (G80, G160, and G240). All plots follow the same bisignate profiles, but the G160 and G240 films show an order of magnitude higher *g*-factor intensity compared to the G80 film, indicating a stronger degree of dissymmetry in the higher spacing films.

observed in both the PEM and the LDLB plots, proving both terms show antisymmetric properties upon sample rotation about their respective dependent axes. The CD contribution from the PEM imperfection is 39 mdeg, which is one-sixth of the LDLB contribution maximum (231 mdeg). Comparing the strength of these terms to the raw and four-scan CD signals (see Figure 5) reveals that the LDLB interaction is the dominant contribution to the raw CD data and can obfuscate the chiroptic-CD contributions in the raw CD signal.

Varying Levels of Structural Order. By controlling the evaporation and deposition process, we make four MSC film samples with different macroscopic ordering, ranging from highly ordered films (linear and radial) to less-ordered films (spin-coated and freely evaporated) (Figure 7a).

The amount of linear order can be quantified through the reduced LD (LD_{red}).[9,34] LD_{red} is calculated by dividing the LD signal by the isotropic absorbance (A). The degree of linear alignment scales directly with LD_{red} ($\frac{LD}{A}$). Plots of LD_{red} (maximum value) show that the linearly and radially aligned films have a single peak aligned with the 324 nm exciton peak, reaching intensities of 0.27 and 0.39, respectively (Figure 7b). In comparison, the less-ordered freely evaporated and spin-coated films have an order of magnitude lower reduced LD intensity (0.04 and 0.03, respectively, at maximum), which correlates to an order of magnitude reduction in linear orientation compared to the radially and linearly aligned films.

Application of the four-scan averaging method removes the LDLB interaction and PEM imperfection contributions to the CD, which enables us to compare the chiroptic-CD signals. Plotting the *g*-factor ($CD_{chiroptic}$ normalized by absorbance), we compare the samples' dissymmetry (Figure 7c). The four-scan averaged *g*-factor data have a similar bisignate profile for all films, but with differing intensity (raw data shown in Figures S8–S10). The bisignate line shape for all the films indicates that the chiroptical signals share the same origin. The linearly aligned film has the strongest *g*-factor with a maximum at 318 nm that is nearly an order of magnitude greater than the maximum of the spin-coated film (0.027 vs 0.003), and, similarly, the minimum of the linearly aligned film is eight times that of the spin-coated film (−0.030 vs −0.0037).

Films produced under controlled evaporation (linearly and radially aligned films) result in higher reduced LD and *g*-factors (dissymmetry) compared to films made under less controlled processes (spin coating and free evaporation) (Figure 7c,d). Of the controlled evaporation films, linearly aligned films have a higher reduced LD and *g*-factor than radially aligned films. The difference in *g*-factor can be caused by (1) dissymmetry anisotropy—the films have different microscopic alignments of the electronic transition dipoles with respect to the measurement direction,[8] or (2) a chiral amplification from changing the cluster-to-cluster distance or the dihedral angle between clusters inside the helical filament.[2] These results indicate that the difference in the macro-assembly process can significantly affect the microstructure of the clusters.

Additionally, typical *g*-factors for chiral inorganic nanostructures such as chiral HgS and Au nanocrystals are between 10^{-4} to 10^{-2}.[35−37] For semiconductor nanocrystals, only a few top-performing optically active materials report *g*-factors above 0.02.[38−41] One of our highly processed linear films presents a g-factor of 0.05 (represented in Figure 7d and Figure S11), which is among the highest reported for semiconducting chiral nanostructures.

https://doi.org/10.1021/acsnano.2c06730
ACS Nano 2022, 16, 20457−20469

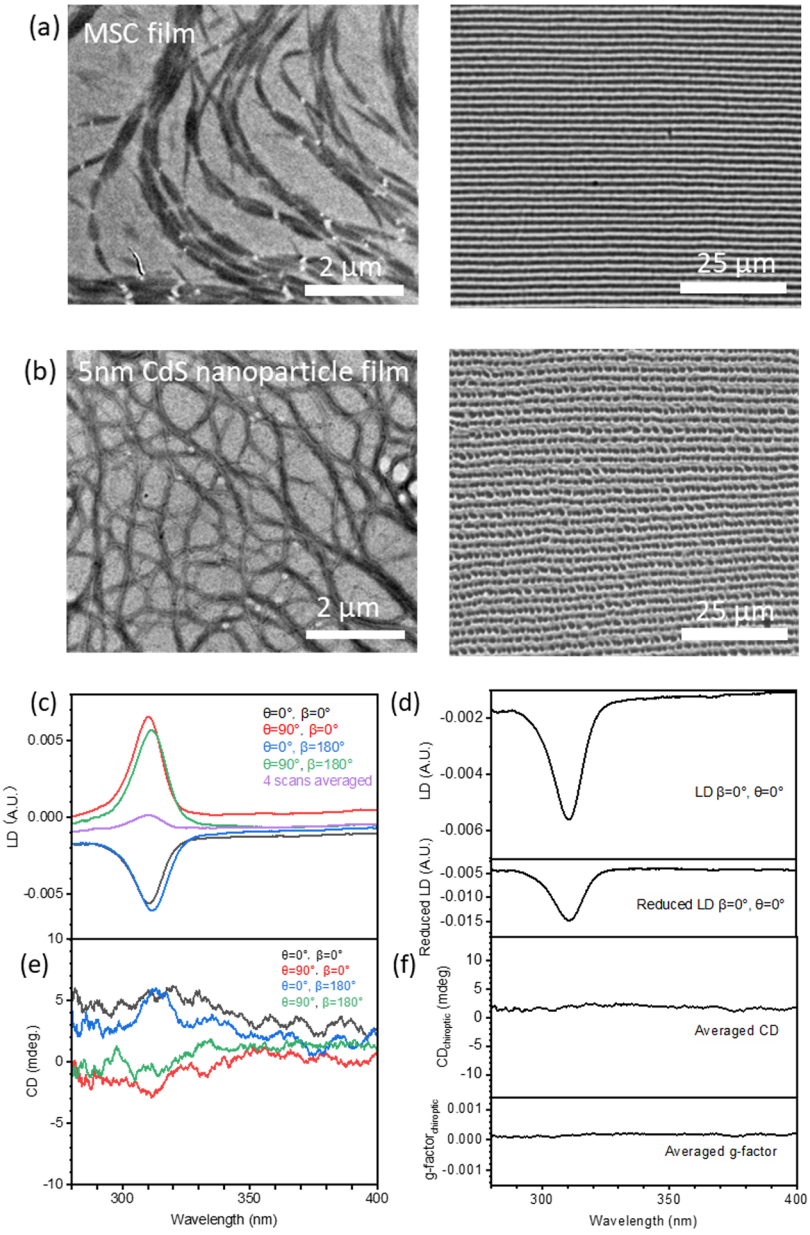

Figure 9. Comparison of hierarchical structure and four-scan CD LD results between linearly aligned 5 nm CdS nanoparticle films and MSC films. (a, b) TEM (left) and optical micrographs (right) at μm and mm scales for MSC linear film (a) and 5 nm nanoparticle film (b), showing similar fibrous networks that lead to linear structures. Nanofilaments are in the sub-μm scale and linearly aligned patterns in the μm−mm scales. (c) Raw and four-scan and averaged LD spectra for the CdS nanoparticle film. Before averaging, angular-dependent LD is observed with peak intensities between 0.006 to −0.0055. The four-scan averaged LD signal (purple) has a peak at 310 nm that is significantly reduced to 0.0002. (d) Top: LD spectra at $\theta = 0°$, $\beta = 0°$ as measured and reduced LD. The reduced LD reaches a peak value of −0.015, indicating linear order. (e) Raw four scan CD spectra for the CdS nanoparticle film. (f) Four-scan averaged CD spectra and *g*-factor for the CdS nanoparticle film. The averaged CD and *g*-factor show only noise, indicating an achiral structure.

Chiroptic Dependence on Evaporation Gap. By examining linearly aligned films made from the same solution but with different evaporation gaps, we find MSC films with the same linear order can demonstrate drastically different *g*-factors, which indicates factors other than linear order can affect the $CD_{chiroptical}$ signal.

We study linearly aligned films made with evaporation gap of 80 μm, 160 μm, and 240 μm (referred as G80, G160, G240). Larger evaporation gaps increase both the film thickness (0.3, 0.6, and 1.0 μm, respectively) and evaporation rate (Figure 8a, Figures S12 and S13, details in Supporting Information). All three films exhibit similar linear patterns, with well-formed bands having a spacing of 3.6 μm (G80) to 4.9 μm (G160 and G240) between bands (Figure 8a right). Their linear orders, however, are varied: the G160 linearly aligned film has the highest order (maximum $LD_{red} = 0.50$) and the G80 and G240 films demonstrate lower but similar order values of 0.21 and 0.27 (Figure 8b, LD_{red} taken at $\theta = 0°$ at $\beta = 0°$). Comparing the *g*-factor values (Figure 8c) (extracted using the four-scan method, full data in Figure S12), we find that the chiroptic-CD signals share the same bisignate line shape with a positive maximum at 318 nm and a negative maximum at 330 nm. The *g*-factor, however, is an order of magnitude larger for the two thicker films (G160 and G240 films) compared to the thinnest

https://doi.org/10.1021/acsnano.2c06730
ACS Nano 2022, 16, 20457−20469

film (G80 film); specifically, the G240 film has an order of magnitude higher *g*-factor than the G80 film in both the positive (−0.027 vs −0.002) and negative (−0.0310 vs −0.0025) peaks. It is interesting to note the G80 and G240 films have similar LD_{red} values (22% difference) but a 10-fold difference in the dissymmetry factors. Reduced LD is an indication of microscopic alignment of electronic dipoles. Hence, the fact the G80 and G240 films have a similar reduced LD and ∼10× difference in *g*-factor indicates there is a large difference in chirality between the two films.

It is important to note for absorbing entities with sizes approaching ∼1/20 of the incident wavelength, light−matter interactions cause preferential scattering of left- or right-handed polarized light (circular differential scattering, CDS) that can be a possible contributor to the CD spectra.[2,42,43] This spurious contribution to the CD spectra has accounted for previously reported increases in *g*-factor as a function of film thickness.[44,45] We believe the order of magnitude difference in the *g*-factor between the linearly aligned films in this study is not caused by CDS due to two reasons. First, the thickness does not directly correlate with the *g*-factor changes (thicknesses are 0.3 μm, 0.6 μm, 1.0 μm for the G80, G160, and G240 films, respectively, and the absorbance relation is graphed in Figures S13 and S14). For example, the G160 film is two times thicker than the G80 film and has a 10 times higher *g*-factor. However, the G160 and G240 films have a ∼ 67% difference in film thickness but similar *g*-factors. Second, our spectra do not display the long-wavelength tailing, which is a typical indication of CDS.[2,46]

Linearly Aligned 5 nm CdS Nanoparticle Film. In this study, we examine how the chiral/achiral nature of the inorganic unit, the organic ligands, and the centimeter-to-millimeter-scale macro-assembly contribute to the chiroptic-CD. To investigate the question above, we characterize aligned films made from large 5 nm CdS nanoparticles (TEM images shown in Figure S15) that share the same organic ligands as the MSC but have a known achiral inorganic core.

TEM and optical micrographs show the nanoparticles form a network structure in the submicron scale. Under controlled evaporation, a millimeter-scale linearly aligned film is fabricated, similar to that of the linearly aligned MSC film (Figure 9a,b, right). The raw LD spectrum features a peak at 310 nm with a maximum intensity of 0.005, indicating linear ordering (Figure 9c). The reduced LD, measured at $\theta = 0°$, $\beta = 0°$, has a peak of −0.015 (Figure 9d), which is an order of magnitude lower than the linear MSC film (Figure 7b). The plot of the four-scan averaged CD signal for the CdS nanoparticle film has high noise between −3 and 5 mdeg and no pronounced features (Figure 9e). The *g*-factor is flat and at the noise level for the system (on the order of 10^{-5}, two orders of magnitude lower than the *g*-factor in all MSC films) (Figure 9f). The lack of CD signal for the 5 nm CdS linearly aligned nanoparticle film indicates the chiroptical signal of our MSC films do not come from the centimeter-to-millimeter-scale filament arrangements or the oleic acid ligand itself.

Origin of the Chiroptic Properties in MSC Films. In general, there are five major mechanisms that produce a signal in a CD spectrometer, recording the differential absorption between left- and right-handed circularly polarized light. These sources of CD are (1) chiral atomic structure, (2) chiral surface structure or chiral ligands on an inorganic core, (3) helical assemblies of nanoparticles, (4) LDLB contributions as outlined in section 2, and/or (5) anisotropic alignment (ordered orientation) of the transition dipoles.[2,8,17] The previous sections with derivations and studies now enable us to eliminate many of these effects as the source for the CD signals in our MSC films.

Working backward, contribution #5, orientational dissymmetry, can be eliminated by the linearly aligned film evaporation geometry study (Figure 8). Results of this study show that two films with the similar level of linear ordering (measured through the same optical axis) can have a drastically different chiroptic-CD signal. Since the reduced LD is an indication of microscopic electronic transition dipole alignment, this study directly compares two films with similar levels of orientational dissymmetry and finds large differences in their chiroptic-CD signal, enabling us to rule out orientational dissymmetry as the cause for the increased chiroptic signals. For contribution #4, the LDLB effect, we have eliminated this through the four-scan averaging method. For contribution #2, surfaces and ligands, we can eliminate the macroscopic fiber and the surface ligands as sources for the chiroptic-CD signal from our analysis of the linearly aligned CdS nanoparticle film (Figure 9). In these studies, the oleic acid ligands bind these larger nanoparticles together and organize them to form linear patterns, but there is no chiroptic-CD signal. Thus, the organic ligands themselves are not the contributors to the chiroptic-CD, and neither is the conformation of the carboxylic acid on the nanoparticles. Concerning surface atom contributions, while there may be chiral inorganic surface structure, it is highly unlikely that these surfaces could dynamically rearrange to modify the intensity of the CD signal as strongly as our studies demonstrate, nor would we expect that any surfaces rearrangements would maintain similar line shapes.

This leaves us with CD contributions from the atomic structure (#1) and from helical arrangements of the MSCs (#3). There is strong evidence for the helical arrangements: all CD profiles from the films, including those with different macroscopic orderings (Figure 7), share the same bisignate CD profile, with the zero-point aligned with the 324 nm MSC absorption peak. A couplet's center aligned with the absorbance peak strongly suggests an exciton-coupled or coupled-oscillator system.[47,48] Additionally, in an exciton coupled system, the increased chiroptic signal can be directly attributed to enhanced coupling from a change to the cluster-to-cluster distance or to the dihedral angle between electronic transition dipoles,[17,24,49] as nicely shown in recent reviews.[2,47,48] These changes would be brought about by the different evaporative processing conditions. As for the core, the results of this work do not confirm or refute the chirality of the core. Considering the clusters are the building blocks of a chiral assembly, they may have an intrinsic chirality or an induced chirality from the self-assembly process. In summary, the source of the chiroptic-CD in the hierarchically structured CdS magic-sized cluster films are from the inorganic core and/or a helical arrangement of the clusters.

Turning our attention toward potential sources for the chiral amplification that is seen between different evaporation processing, we postulate that there are some solid−solid interactions during film formation that can influence the helical arrangements, potentially "twisting" the filaments to a greater or lesser degree with concomitant changes in the *g*-factor intensity. A clear trend emerges when the *g*-factor is juxtaposed against the reduced LD for samples with different macroscopic patterning (Figure 7d): films made under controlled evaporation have a higher reduced LD and higher *g*-factor.

https://doi.org/10.1021/acsnano.2c06730
ACS Nano 2022, 16, 20457−20469

The increased linear order in the radially and linearly aligned films is due to a more aligned microstructure from controlled evaporation, as compared to the unconfined conditions for the spin-coated and freely evaporated films. To probe the fine structure of the assembly, we have delaminated spin coated and linearly aligned MSC films with thiols and characterized them using scanning electron microscopy (SEM) (Figure S16, and experimental details in Supporting Information). For the linearly aligned film, we observe linear bands that are partially delaminated into individual fibers. Magnified images of the fiber show it is formed by the helical twisting of smaller filaments (~20 nm in diameter). As a control sample, the spin coated film displays local cracking after thiol treatment with little evidence of filament twisting. The comparison between the linearly aligned and spin coated film implies the chiral amplification observed in the controlled evaporation film is caused by the increased angular alignment between adjoining MSCs inside the filament.

To be noted, CD that emanates from a system of aligned analytes is anisotropic: the increasing *g*-factor can also be a result of the difference in local ordering/orientation of the analytes with respect to the light direction (dissymmetry anisotropy).[42] In the spacing studies (Figure 8), we can identify the change in *g*-factor between G80 and G240 films as chirality amplification since they share the same reduced LD (same microscopic electronic transition dipole alignment). The chirality amplification is likely caused by the larger evaporation spacing that leads to a faster evaporation speed and a greater propensity for fiber−fiber or fiber-substrate interactions during the evaporative assembly process. These interactions result in a higher torque being placed on the fiber from filament-filament twisting, from pinning of one side of a fiber to the glass, or from another unidentified source (Figure S16). The faster evaporation rate leads to a stronger torque, which then results in increased chirality (Figure 8).

CONCLUSIONS

In this paper, we derive and demonstrate a method to extract chiroptic-CD signals from linear anisotropic effects by averaging four measurements—two measurements along the azimuthal angles (0° and 90°) and two measurements along the vertical axis perpendicular to the beam direction (0° and 180°). We show that taking two measurements at 0° and 90° azimuthal angles instead of multiple scans at 15° increments is sufficient to remove the CD signal from PEM imperfection. Application of our method to MSC films with different macroscopic orderings shows that they share the same exciton-coupled chiroptic-CD profile but with varying signal intensity. The films produced under controlled evaporation processing possess a higher reduced LD and *g*-factor, which indicates the dissymmetry is dependent on the film assembly process. Additionally, we achieve a controllable level of cluster assembly chirality by changing the evaporation geometry. Our linearly aligned MSC film produces a *g*-factor of 0.05, which is among the highest values reported for all semiconductor chiral nanostructures. Through our systematic studies, we can eliminate several sources for the chiroptic-CD signals, confirming that chirality originates from a chiral MSC assembly or the inorganic MSC cores. As the building block of the chiral assembly, the MSC may have intrinsic or induced chirality from the assembly twisting. Our study establishes a method to reliably extract the optical dissymmetry from a complex hierarchical nanostructure, demonstrating a controllable amount of dissymmetry and setting the stage for future research in harnessing and characterizing self-assembled nanostructures in chiroptical applications.

METHODS/EXPERIMENTAL SECTION

CD and LD Measurements. All measurements were conducted using a JASCO J-1500 CD spectrometer with a custom-made 2.5 mm diameter circular aperture. MSC and nanoparticle films preparations: The linearly aligned magic-sized cluster (MSC) film was produced through controlled evaporation where we drop-cast 7 μL of 20 mg/mL MSC/hexane solution (stirred clockwise for 2 days) on a glass slide and then capped the droplet with another glass slide. Double sided tape was used as a spacer and to seal off three sides of the glass slides, only allowing evaporation through one direction. The radially aligned MSC film was produced in the same fashion except the double-sided tapes were cut into smaller pieces, allowing evaporation through all directions. The spin-coated film was made by rotating a 5 mg/mL MSC/hexane solution at 1000 rpm for 5 min. The freely evaporated films were created by drop-casting 10 μL of 20 mg/mL MSC/hexane solution on a glass slide and allowing it to evaporate without a cover glass slide. The linearly aligned 5 nm CdS nanoparticle film was made using the same method as the linearly aligned MSC film, except the CdS nanoparticle is mixed with cadmium oleate in a 1:1 weight ratio to facilitate the self-assembly during evaporation. High-angle annular dark-field scanning transmission electron microscopy (HAADF-STEM): HAADF images were acquired using an Thermo Fisher Scientific-Titan electron microscope operated at 200 kV. The samples were prepared by drop-casting a solution of MSCs in hexane on an ultrathin carbon film grid (precleaned) followed by a beam shower. Small angle X-ray scattering (SAXS): SAXS experiments were conducted on linearly aligned MSC film using Rigaku PSAXS-L to explore a Q range between 0.05 A^{-1} to 0.81 A^{-1}. Optical microscopy: Optical micrographs were collected using an Olympus BX51 cross-polarized microscope. Linear polarizers were placed before and after the glass slide samples, perpendicular to one another.

ASSOCIATED CONTENT

Supporting Information

The Supporting Information is available free of charge at https://pubs.acs.org/doi/10.1021/acsnano.2c06730.

Detailed description of the experimental method, full Mueller matrix derivation on lock-in amplifier operation and CD, LD raw data from the application of the four-scan method to all samples mentioned in the manuscript (PDF)

AUTHOR INFORMATION

Corresponding Author

Richard D. Robinson − *Department of Materials Science and Engineering, Cornell University, Ithaca, New York 14853, United States; Kavli Institute at Cornell for Nanoscale Science, Ithaca, New York 14853, United States;* orcid.org/0000-0002-0385-2925; Email: rdr82@cornell.edu

Authors

Yuan Yao − *Department of Materials Science and Engineering, Cornell University, Ithaca, New York 14853, United States;* orcid.org/0000-0002-4784-2753

Thomas J. Ugras − *School of Applied and Engineering Physics, Cornell University, Ithaca, New York 14853, United States; Kavli Institute at Cornell for Nanoscale Science, Ithaca, New York 14853, United States;* orcid.org/0000-0002-5931-3031

https://doi.org/10.1021/acsnano.2c06730
ACS Nano 2022, 16, 20457−20469

Talisi Meyer − *Department of Materials Science and Engineering, Cornell University, Ithaca, New York 14853, United States*

Matthew Dykes − *Department of Physics, Cornell University, Ithaca, New York 14853, United States;* orcid.org/0000-0001-8777-0929

Da Wang − *Electron Microscopy for Materials Science (EMAT) and NANOlab Center of Excellence, University of Antwerp, 2020 Antwerp, Belgium*

Arantxa Arbe − *Centro de Física de Materiales (CSIC, UPV/EHU) and Materials Physics Center MPC, E-20018 San Sebastián, Spain*

Sara Bals − *Electron Microscopy for Materials Science (EMAT) and NANOlab Center of Excellence, University of Antwerp, 2020 Antwerp, Belgium;* orcid.org/0000-0002-4249-8017

Bart Kahr − *Department of Chemistry and Molecular Design Institute, New York University, New York City, New York 10003, United States*

Complete contact information is available at: https://pubs.acs.org/10.1021/acsnano.2c06730

Notes

The authors declare no competing financial interest.

ACKNOWLEDGMENTS

This work was supported in part by the National Science Foundation (NSF) under Award Nos. DMR-2003431 and CHE-2003586. This work made use of the Cornell Center for Materials Research Shared Facilities, which are supported through the NSF MRSEC program (DMR-1719875). This work is partly supported by Grant PID2021-123438NB-I00 (MCIN/AEI/10.13039/501100011033 and "ERDF A way of making Europe") and Grant IT1566-22 (Eusko Jaurlaritza). D.W. acknowledges an Individual Fellowship funded by the Marie Sklodowska-Curie Actions (MSCA) in the Horizon 2020 program (Grant 894254 SuprAtom). S.B. acknowledges financial support from ERC Consolidator Grant No. 815128 REALNANO. B.K. acknowledges NSF award DMR-2003968. We would like to thank Dr. Mark August Pfeifer for help with circular dichroism measurements. Additionally, we would like to thank Professor Luis M. Liz-Marzán for invaluable discussions on chirality.

REFERENCES

(1) Ma, W.; Xu, L.; de Moura, A. F.; Wu, X.; Kuang, H.; Xu, C.; Kotov, N. A. Chiral Inorganic Nanostructures,. *Chem. Rev.* **2017**, *117* (12), 8041−8093.

(2) Albano, G.; Pescitelli, G.; Di Bari, L. Chiroptical Properties in Thin Films of π-Conjugated Systems,. *Chem. Rev.* **2020**, *120* (18), 10145−10243.

(3) Kumar, J.; Liz-Marzán, L. M. Recent Advances in Chiral Plasmonics — Towards Biomedical Applications,. *Bull. Chem. Soc. Jpn.* **2019**, *92* (1), 30−37.

(4) Zhiyong, T.; Zhengtao, L.; Lin, S.; Zhiyong, T.; Wei, Z.; Chengyi, S.; Chen, Z.; Peng, T.; Assaf Ben, M.; Gil, M.; Chenjie, Z.; Zhikun, W.; Rongchao, J.; Yuanyuan, C.; Shunai, C.; Hua, K.; Chuanlai, X.; Tomohiro, Y.; Hiroyuki, M.; Shu, K.*Chiral Nanomaterials: Preparation, Properties and Applications*, 1st ed.; Wiley-VCH Verlag GmbH & Co. KGaA: Weinheim, Germany, 2018. DOI: 10.1002/9783527682782.

(5) Ben-Moshe, A.; Maoz, B. M.; Govorov, A. O.; Markovich, G. Chirality and chiroptical effects in inorganic nanocrystal systems with plasmon and exciton resonances,. *Chem. Soc. Rev.* **2013**, *42* (16), 7028.

(6) Aiello, C. D.; Abendroth, J. M.; Abbas, M.; Afanasev, A.; Agarwal, S.; Banerjee, A. S.; Beratan, D. N.; Belling, J. N.; Berche, B.; Botana, A.; Caram, J. R.; Celardo, G. L.; Cuniberti, G.; Garcia-Etxarri, A.; Dianat, A.; Diez-Perez, I.; Guo, Y.; Gutierrez, R.; Herrmann, C.; Hihath, J.; et al. A Chirality-Based Quantum Leap,. *ACS Nano* **2022**, *16* (4), 4989−5035.

(7) Claborn, K.; Isborn, C.; Kaminsky, W.; Kahr, B. Optical Rotation of Achiral Compounds,. *Angew. Chem., Int. Ed.* **2008**, *47* (31), 5706−5717.

(8) Martin, A. T.; Nichols, S. M.; Murphy, V. L.; Kahr, B. Chiroptical Anisotropy of Crystals and Molecules,. *Chem. Commun.* **2021**, *57*, 8107−8120.

(9) Berova, N.; Polavarapu, P. L.; Nakanishi, K.; Woody, R. W.*Comprehensive Chiroptical Spectroscopy*, 1st ed.; John Wiley & Sons, Inc: Hoboken, NJ, 2012; Vol. 1: Instrumentation, Methodologies, and Theoretical Simulations.

(10) Shindo, Y.; Nishio, M. The effect of linear anisotropies on the CD spectrum: Is it true that the oriented polyvinylalcohol film has a magic chiral domain inducing optical activity in achiral molecules? *Biopolymers* **1990**, *30*, 25−31.

(11) Albano, G.; Górecki, M.; Jávorfi, T.; Hussain, R.; Siligardi, G.; Pescitelli, G.; Di Bari, L.Spatially resolved chiroptical study of thin films of benzo[1,2-b:4,5-b']dithiophene-based oligothiophenes by synchrotron radiation electronic circular dichroism imaging (SR-ECDi) technique.*Aggregate***2022**, *3* (5) DOI: 10.1002/agt2.193.

(12) Wolffs, M.; George, S. J.; Tomović, Ž.; Meskers, S. C. J.; Schenning, A. P. H. J.; Meijer, E. W. Macroscopic Origin of Circular Dichroism Effects by Alignment of Self-Assembled Fibers in Solution,. *Supramol. Chem.* **2007**, *46*, 8203−8205.

(13) Schellman, J.; Jensen, H. P. Optical spectroscopy of oriented molecules. *Chem. Rev.* **1987**, *87* (6), 1359−1399.

(14) Shindo, Y.; Ohmi, Y. New polarization-modulation spectrometer for simultaneous circular dichroism and optical rotary dispersion measurements (I): Instrument design, analysis, and evaluation,. *Rev. Sci. Instrum.* **1985**, *56* (12), 2237−2242.

(15) Kuroda, R.; Harada, T.; Shindo, Y. A solid-state dedicated circular dichroism spectrophotometer: Development and application,. *Rev. Sci. Instrum.* **2001**, *72* (10), 3802−3810.

(16) von Weber, A.; Hooper, D. C.; Jakob, M.; Valev, V. K.; Kartouzian, A.; Heiz, U. Circular Dichroism and Isotropy - Polarity Reversal of Ellipticity in Molecular Films of 1,1'-Bi-2-Naphtol,. *ChemPhysChem* **2019**, *20* (1), 62−69.

(17) Guerrero-Martínez, A.; Auguié, B.; Alonso-Gómez, J. L.; Džolić, Z.; Gómez-Graña, S.; Žinić, M.; Cid, M. M.; Liz-Marzán, L. M. Intense Optical Activity from Three-Dimensional Chiral Ordering of Plasmonic Nanoantennas,. *Angew. Chem., Int. Ed.* **2011**, *50* (24), 5499−5503.

(18) Tunis-Schneider, M. J. B.; Maestre, M. F. Circular dichroism spectra of oriented and unoriented deoxyribonucleic acid films-A preliminary study,. *J. Mol. Biol.* **1970**, *52* (3), 521−541.

(19) Szustakiewicz, P.; Kowalska, N.; Grzelak, D.; Narushima, T.; Góra, M.; Bagiński, M.; Pociecha, D.; Okamoto, H.; Liz-Marzán, L. M.; Lewandowski, W. Supramolecular Chirality Synchronization in Thin Films of Plasmonic Nanocomposites,. *ACS Nano* **2020**, *14* (10), 12918−12928.

(20) Liu, Y.-H.; Wang, F.; Wang, Y.; Gibbons, P. C.; Buhro, W. E. Lamellar Assembly of Cadmium Selenide Nanoclusters into Quantum Belts,. *J. Am. Chem. Soc.* **2011**, *133* (42), 17005−17013.

(21) Shukla, N.; Gellman, A. J. Chiral metal surfaces for enantioselective processes,. *Nat. Mater.* **2020**, *19* (9), 939−945.

(22) Puri, M.; Ferry, V. E. Circular Dichroism of CdSe Nanocrystals Bound by Chiral Carboxylic Acids,. *ACS Nano* **2017**, *11* (12), 12240−12246.

(23) Qian, H.; Eckenhoff, W. T.; Zhu, Y.; Pintauer, T.; Jin, R. Total Structure Determination of Thiolate-Protected Au_{38} Nanoparticles,. *J. Am. Chem. Soc.* **2010**, *132* (24), 8280−8281.

(24) Fan, Z.; Govorov, A. O. Plasmonic Circular Dichroism of Chiral Metal Nanoparticle Assemblies,. *Nano Lett.* **2010**, *10* (7), 2580−2587.
(25) Wade, J.; Hilfiker, J. N.; Brandt, J. R.; Liirò-Peluso, L.; Wan, L.; Shi, X.; Salerno, F.; Ryan, S. T. J.; Schöche, S.; Arteaga, O.; Jávorfi, T.; Siligardi, G.; Wang, C.; Amabilino, D. B.; Beton, P. H.; Campbell, A. J.; Fuchter, M. J. Natural optical activity as the origin of the large chiroptical properties in π-conjugated polymer thin films,. *Nat. Commun.* **2020**, *11* (1), 6137.
(26) Nevers, D. R.; Williamson, C. B.; Savitzky, B. H.; Hadar, I.; Banin, U.; Kourkoutis, L. F.; Hanrath, T.; Robinson, R. D. Mesophase Formation Stabilizes High-Purity Magic-Sized Clusters,. *J. Am. Chem. Soc.* **2018**, *140* (10), 3652−3662.
(27) Han, H.; Kallakuri, S.; Yao, Y.; Williamson, C. B.; Nevers, D. R.; Savitzky, B. H.; Skye, R. S.; Xu, M.; Voznyy, O.; Dshemuchadse, J.; Kourkoutis, L. F.; Weinstein, S. J.; Hanrath, T.; Robinson, R. D. Multiscale hierarchical structures from a nanocluster mesophase,. *Nat. Mater.* **2022**, *21*, 518−525.
(28) Arteaga, O.; Freudenthal, J.; Wang, B.; Kahr, B. Mueller matrix polarimetry with four photoelastic modulators: Theory and calibration,. *Appl. Opt.* **2012**, *51* (28), 6805−6817.
(29) Jones, R. C. A New Calculus for the Treatment of Optical Systems. VII. Properties of the N-Matrices. *J. Opt. Soc. Am.* **1948**, *38*, 671−685.
(30) Azzam, R. M. A. Propagation of partially polarized light through anisotropic media with or without depolarization: A differential 4X4 matrix calculus,. *J. Opt. Soc. Am.* **1978**, *68* (12), 1756−1767.
(31) Jensen, H. P.; Schellman, J. A.; Troxell, T. Modulation Techniques in Polarization Spectroscopy.,. *Appl. Spectrosc.* **1978**, *32* (2), 192−200.
(32) Salij, A.; Goldsmith, R. H.; Tempelaar, R. Theory of Apparent Circular Dichroism Reveals the Origin of Inverted and Noninverted Chiroptical Response under Sample Flipping,. *J. Am. Chem. Soc.* **2021**, *143* (51), 21519−21531.
(33) Zhou, K.; Simpson, G.; Chen, X.; Zhang, L.; Bennion, I. High extinction ratio in-fiber polarizers based on 45° tilted fiber Bragg gratings,. *Opt. Lett.* **2005**, *30* (11), 1285−1287.
(34) Rajendra, J.; Baxendale, M.; Dit Rap, L. G.; Rodger, A. Flow Linear Dichroism to Probe Binding of Aromatic Molecules and DNA to Single-Walled Carbon Nanotubes,. *J. Am. Chem. Soc.* **2004**, *126* (36), 11182−11188.
(35) Wang, P.; Yu, S.-J.; Govorov, A. O.; Ouyang, M. Cooperative expression of atomic chirality in inorganic nanostructures. *Nat. Commun.* **2017**, *8*, 14312.
(36) Vestler, D.; Ben-Moshe, A.; Markovich, G. Enhancement of Circular Dichroism of a Chiral Material by Dielectric Nanospheres,. *J. Phys. Chem. C* **2019**, *123*, 5017.
(37) Lee, H.-E.; Kim, R. M.; Ahn, H.-Y.; Lee, Y. Y.; Byun, G. H.; Im, S. W.; Mun, J.; Rho, J.; Nam, K. T. Cysteine-encoded chirality evolution in plasmonic rhombic dodecahedral gold nanoparticles,. *Nat. Commun.* **2020**, *11* (263), 1−10.
(38) Yeom, J.; Yeom, B.; Chan, H.; Smith, K. W.; Dominguez-Medina, S.; Bahng, J. H.; Zhao, G.; Chang, W.-S.; Chang, S. J.; Chuvilin, A.; Melnikau, D.; Rogach, A. L.; Zhang, P.; Link, S.; Král, P.; Kotov, N. A. Chiral Templating of Self-Assembling Nanostructures by Circularly Polarized Light,. *Nat. Mater.* **2015**, *14* (1), 66.
(39) Yeom, J.; Santos, U. S.; Chekini, M.; Cha, M.; de Moura, A. F.; Kotov, N. A. Chiromagnetic nanoparticles and gels,. *Science* **2018**, *359* (6373), 309−314.
(40) Chen, L.; Hao, C.; Cai, J.; Chen, C.; Ma, W.; Xu, C.; Xu, L.; Kuang, H. Chiral Self-Assembled Film from Semiconductor Nanorods with Ultra-Strong Circularly Polarized Luminescence,. *Angew. Chem., Int. Ed.* **2021**, *60* (50), 26276−26280.
(41) Duan, Y.; Liu, X.; Han, L.; Asahina, S.; Xu, D.; Cao, Y.; Yao, Y.; Che, S. Optically Active Chiral CuO 'Nanoflowers,'. *J. Am. Chem. Soc.* **2014**, *136* (20), 7193−7196.
(42) Bustamante, C.; Tinoco, I.; Maestre, M. F. Circular differential scattering can be an important part of the circular dichroism of macromolecules.,. *Proc. Natl. Acad. Sci. U. S. A.* **1983**, *80* (12), 3568−3572.
(43) Jiang, S.; Kotov, N. A. Circular Polarized Light Emission in Chiral Inorganic Nanomaterials. *Adv. Mater.* **2022**, 1−19.
(44) Craig, M. r.; Jonkheijm, P.; Meskers, S. c. j.; Schenning, A. p. h. j.; Meijer, E. w. The Chiroptical Properties of a Thermally Annealed Film of Chiral Substituted Polyfluorene Depend on Film Thickness,. *Adv. Mater.* **2003**, *15* (17), 1435−1438.
(45) Lakhwani, G.; Meskers, S. C. J.; Janssen, R. A. J. Circular Differential Scattering of Light in Films of Chiral Polyfluorene,. *J. Phys. Chem. B* **2007**, *111* (19), 5124−5131.
(46) Oda, M.; Nothofer, H.-G.; Scherf, U.; Sunjic, V.; Richter, D.; Regenstein, W.; Neher, D. Chiroptical properties of chiral-substituted polyfluorenes,. *Macromolecules* **2002**, *35* (18), 6792−6798.
(47) Telfer, S. G.; McLean, T. M.; Waterland, M. R. Exciton coupling in coordination compounds,. *Dalton Trans.* **2011**, *40* (13), 3097−3108.
(48) Rodger, A.; Marshall, D. Beginners guide to circular dichroism,. *Biochem* **2021**, *43* (2), 58−64.
(49) Norman, P.; Linares, M. On the Interplay Between Chirality and Exciton Coupling: A DFT Calculation of the Circular Dichroism in π-Stacked Ethylene,. *Chirality* **2014**, *26* (9), 483−489.

https://doi.org/10.1021/acsnano.2c06730
ACS Nano 2022, 16, 20457−20469